ADVANCED FUNCTIONAL MATERIALS
www.afm-journal.de

High-Performance Inverted Polymer Solar Cells: Device Characterization, Optical Modeling, and Hole-Transporting Modifications

*Jingyu Zou, Hin-Lap Yip, Yong Zhang, Yan Gao, Shang-Chieh Chien, Kevin O'Malley, Chu-Chen Chueh, Hongzheng Chen, and Alex K.-Y. Jen**

Although high power conversion efficiencies (PCE) have already been demonstrated in conventional structure polymer solar cells (PSCs), the development of high performance inverted structure polymer solar cells is still lagging behind despite their demonstrated superior stability and feasibility for roll-to-roll processing. To address this challenge, a detailed study of solution-processed, inverted-structure PSCs based on the blends of a low bandgap polymer, poly(indacenodithiophene-*co*-phananthrene-quinoxaline) (PIDT-PhanQ) and [6,6]-phenyl-C_{71}-butyric acid methyl ester ($PC_{71}BM$) as the bulk heterojunction (BHJ) layer is carried out. Comprehensive characterization and optical modeling of the resulting devices is performed to understand the effect of device geometry on photovoltaic performance. Excellent device performance can be achieved by optimizing the optical field distribution and spatial profiles of excitons generation within the active layer in different device configurations. In the inverted structure, because the peak of the excitons generation is located farther away from the electron-collecting electrode, a higher blending ratio of fullerene is required to provide higher electron mobility in the BHJ for achieving good device performance.

1. Introduction

Polymer solar cells (PSCs) have gained significant interest as a promising technology for renewable energy due to their potential for low-cost, light-weight, and roll-to-roll processing on flexible substrates.[1–5] In most cases, PSCs based on the conventional device structure are fabricated by sandwiching an active layer between a low work-function metal cathode (e.g., Ca/Al) and a transparent indium tin oxide (ITO) anode with a conducting polymer, poly(3,4-ethylenedioxylenethiophene):poly(styrenesulfonic acid) (PEDOT:PSS) usually used as an anode buffer layer. A bulk-heterojunction (BHJ) active layer often consists of a blend of an electron-rich conjugated polymer donor and an electron-deficient fullerene acceptor to form a bicontinuous interpenetrating network. Recently, the newly developed low bandgap polymers[6–12] and fullerene derivatives[13] have enabled the fabrication of very high power conversion efficiencies (PCEs) of >7% in the conventional structure PSCs.

However, long-term stability of these devices in ambient conditions is a major concern. The commonly used low work function cathode, such as calcium or aluminum, is easily oxidized under ambient conditions. In addition, ITO can be etched easily by very acidic PEDOT:PSS to cause device degradation.[14] One way to circumvent these problems is to use an inverted structure PSC. By reversing the polarity of charge collection in the conventional structure, the inverted structure allows more air stable, higher work function metals (e.g., Ag, Cu)[15] to be used in combination with an appropriate interfacial layer (e.g., PEDOT:PSS, MoO_3, V_2O_5, graphene oxide (GO)) to collect holes,[16–20] while a transparent electrode in combination with a metal oxide (e.g., TiO_x, ZnO, Cs_2CO_3) could be used to collect electrons.[19,21–24]

Previously, we have demonstrated that high efficiency inverted devices with good ambient stability could be achieved in the BHJ layer made of poly(3-hexylthiophene) (P3HT) and [6,6] phenyl-C_{61}-butyric acid methyl ester ($PC_{61}BM$).[16] Since then, numerous studies have been conducted on the same active material system trying to develop a deeper understanding of the effect of the interface,[16,25–28] optical field distribution,[29–31] and vertical phase separation in the BHJ active layer on device performance.[32] Because of the intrinsic limitation of light harvesting in the P3HT/$PC_{61}BM$ system, the PCE of most of the inverted structure PSCs studied so far are in the range of 3–4%, which are lower than those obtained from conventional PSCs.[33,34]

J. Y. Zou, Dr. H.-L. Yip, Dr. Y. Zhang, Y. Gao, S.-C. Chien, K. O'Malley, C.-C. Chueh, Prof. H. Chen, Prof. A. K.-Y. Jen
Department of Materials Science and Engineering
University of Washington
BOX 352120, Seattle, Washington, 98195, USA
E-mail: ajen@u.washington.edu
Y. Gao, Prof. H. Chen
State Key Laboratory of Silicon Materials
MOE Key Laboratory of Macromolecule Synthesis and Functionalization
Zhejiang-California International Nanosystems Institute
Zhejiang University
Hangzhou 310027, P. R. China
K. M. O'Malley, Prof. A. K.-Y. Jen
Department of Chemistry
University of Washington
Box 351700, Seattle, WA 98195, USA

DOI: 10.1002/adfm.201102937

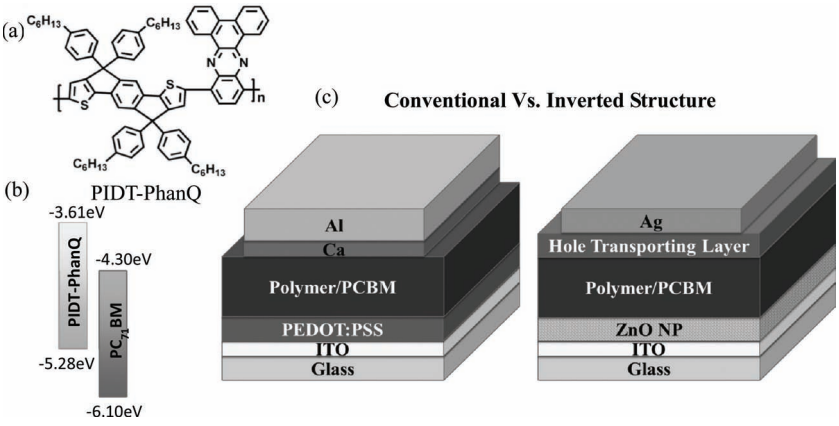

Figure 1. a) The molecular structure of PIDT-PhanQ. b) Energy level diagrams for PIDT-PhanQ and $PC_{71}BM$. c) The device structure of conventional and inverted structure PSCs.

Recently, there are several reports showed inverted devices with >6% PCE could be achieved by incorporating newly developed donors.[35–37] With the rapid development of new polymer donors, there is a substantial room for further improvement of inverted devices. Here, we report the comprehensive study of a series of conventional and inverted structure devices using poly(indacenodithiophene-*co*-phananthrenequinoxaline) (PIDT-PhanQ) and [6,6]-phenyl-C_{71}-butyric acid methyl ester ($PC_{71}BM$) as the active material with different polymer:fullerene blending ratios.

The chemical structure and energy diagram of PIDT-PhanQ and $PC_{71}BM$ are shown in **Figure 1**a,b. Previously, we have shown that the PCE of conventional structure PSCs based on the blend of PIDT-PhanQ and $PC_{71}BM$ can reach over 6% at an optimized 1:3 polymer:fullerene blending ratio.[38] However, a higher fullerene content of 1:4 is needed in the BHJ films of inverted cells in order to achieve higher device efficiency. To better understand the effect of the blend compositions on photovoltaic performance of these device architectures, we have correlated their current–voltage (*J*–*V*) characteristics and external quantum efficiency (EQE) results in conjunction with optical modeling.

The active layers showed similar UV-vis absorption spectra when they were deposited on top of either PEDOT:PSS, as in the conventional structure, or ZnO, as in the inverted structure. However, the results from optical modeling reveal that significant differences in optical distribution and exciton generation profiles between these two device architectures after the complete devices were fabricated by putting on the top electrodes. For the best device in the conventional structure, the peak of the exciton generation profile within the BHJ is located in the middle of the vertical direction of the film. In the inverted structure, the peak of the exciton generation profile is located closer to the top anode. As a result, the majority of electrons in the inverted cell need to travel a longer distance to reach the bottom cathode. Therefore, improvement of the electron mobility in the BHJ is required to achieve optimized performance for inverted cells. This can be achieved by increasing the fullerene to polymer blend ratio from 3:1 to 4:1, which resulted in a factor of 3 increase in electron mobility measured by electron-only devices.

To further improve the efficiency of the inverted cells, we have modified the interface between the PEDOT:PSS hole-transporting layer and the Ag anode with a thin layer of graphene oxide (GO). The use of a GO modifier improves the electron-blocking properties of the anode, which is supported by the decreased dark current under reverse bias. A high PCE of 6.38% was achieved, which is even higher than that of the optimal conventional device.

2. Results and Discussion

Figure 1c depicts the schematics of both the conventional and inverted structure devices. The conventional structure devices use the PEDOT:PSS-coated ITO to collect holes and calcium/aluminum cathode to collect electrons, while the inverted devices use ZnO nanoparticles (ZnO NP) film as the electron-transporting or selecting layer and PEDOT:PSS as the hole-transporting layer. The distribution of optical density in the active layer showed marked differences between these two device architectures. This causes exciton dissociation profile to shift and strongly affects the device performance.

2.1. Devices Characteristics

Composition change of the polymer/$PC_{71}BM$ blend affects the efficiency of light harvesting as well as the balance of charge transfer in the devices. To achieve optimal performance of PIDT-PhanQ/$PC_{71}BM$ based PSCs, a series of conventional and inverted structure devices with different blending ratios were fabricated. Thickness of the active layer was optimized based on the result of the best performance devices derived from previous round of study. The *J*–*V* characteristics of these devices are shown in **Figure 2**a,b and their performance are listed in **Table 1**. The detailed fabrication procedures are described in the Experimental Section.

All photoactive layers in the fabricated devices were ≈90–100 nm in thickness. Similar open-circuit voltages (V_{oc}'s) were observed for all the conventional structure devices, even when the polymer/fullerene ratio was varied from 1:2 to 1:5 in the BHJ layer. However, both the short-circuit current density (J_{sc}) and the fill factor (FF) of the devices increase when the blending ratio was changed from 1:2 to 1:3. When it was further increased to 1:5, the J_{sc} and FF of the devices started to decrease. The devices with the 1:3 blending ratio exhibit the best performance, with J_{sc} of 11.2 mA cm^{-2} and a FF of 64%.[38] When similar processing conditions and blending ratios of the BHJ films were used in the inverted structure devices, a relatively large decrease of PCE from 6.24% to 4.91% was observed. Both J_{sc} and FF in the inverted devices are lower; in particular the FF dropped from 64% to 55%. To achieve better PCE, a systematic tuning of the blending ratio in the BHJ film was performed. The best device performance was obtained when the fullerene content was increased to 80%, which resulted in

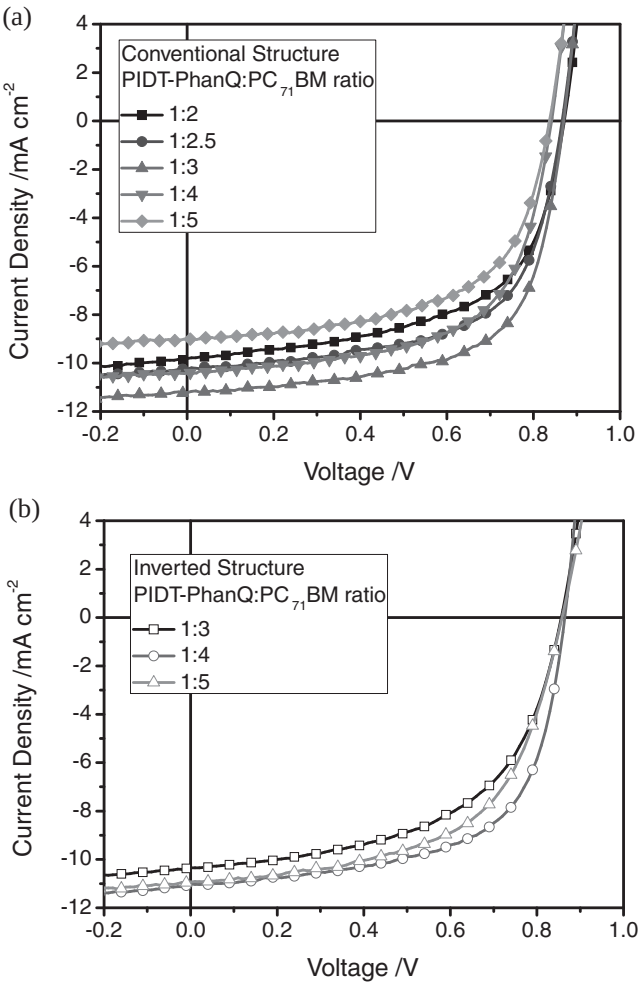

Figure 2. J–V characteristics of a) conventional structure and b) inverted structure PSCs based on PIDT-PhanQ:$PC_{71}BM$ with different blending ratios.

devices with J_{sc} of 11.0 mA cm^{-2}, FF of 64%, and PCE of up to 5.97%. Further increase of the fullerene ratio gave negative effect on both J_{sc} and FF, which led toward a decreased PCE.

Table 1. Performance of conventional and inverted structure devices with different PIDT-PhanQ/$PC_{71}BM$ blending ratios.

Conventional Structure	Ratio	V_{oc} [V]	J_{sc} [mA cm^{-2}]	FF	PCE [%]	J_{max} [mA cm^{-2}]	J_{sc}/J_{max}
	1:2	0.87	9.81	0.58	4.98		
	1:2.5	0.87	10.2	0.62	5.50		
	1:3	0.87	11.2	0.64	6.24	13.0	86%
	1:4	0.84	10.4	0.61	5.41	12.6	83%
	1:5	0.84	9.01	0.59	4.46		
Inverted Structure	Ratio	V_{oc} [V]	J_{sc} [mA cm^{-2}]	FF	PCE (%)	J_{max} [mA cm^{-2}]	J_{sc}/J_{max}
	1:3	0.87	10.4	0.55	4.91	16.5	63%
	1:4	0.86	11.0	0.63	5.97	15.6	71%
	1:5	0.86	10.9	0.58	5.44		

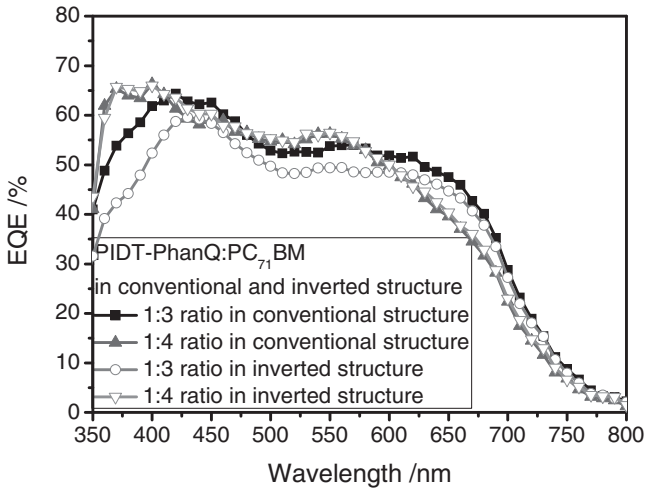

Figure 3. EQE of devices based on conventional and inverted structure with PIDT-PhanQ: $PC_{71}BM$ blending ratios of 1:3 and 1:4.

To compare the device characteristics of PSCs prepared under the same processing condition of the BHJ films in different structures, external quantum efficiencies (EQE) of devices with 1:3 and 1:4 polymer/fullerene blending ratios in both conventional and inverted structures were measured (**Figure 3**). The data showed that for inverted device with a 1:3 blending ratio, the EQE was lower than that of the conventional cell over most of the absorption spectrum, which resulted in lower J_{sc} values. For the one with the 1:4 blending ratio, the EQE was similar to,or slightly higher than that of the conventional cells.

Compared to the EQE spectra of the BHJ films with 1:3 and 1:4 polymer/fullerene blending ratios, the films with 1:3 ratio showed higher EQE in the range between 600 and 700 nm, while the films with a 1:4 ratio gained higher EQE in the ranges of 500–600 nm and 350–400 nm. **Figure 4**a shows the absorption spectra of PIDT-PhanQ:$PC_{71}BM$ BHJ films with different blend compositions on top of the PEDOT or ZnO-coated glass substrates and Figure 4b shows the extinction coefficient (k) of both pure PIDT-PhanQ and $PC_{71}BM$ films obtained from spectroscopic ellipsometry. According to Figure 4, it can be easily explained that films with higher polymer content exhibit higher EQE in the range between 600 and 700 nm due to enhanced contribution from the polymer absorption, while higher $PC_{71}BM$ content in the 1:4 ratio film provides stronger absorption in the ranges between 500–600 nm and 350–400 nm.

2.2. Optical Modeling Characteristics

Since EQE could be affected by several factors, such as rate of photon absorption in the active layer, exciton generation, and charge separation, transport, and collection, to understand the difference of EQE in various device structures with the same composition, one must compare photon absorption in the device active layers. Similar UV-vis absorption spectra were found when the same composition of the BHJ films were deposited on PEDOT:PSS for the conventional structure and on ZnO for the inverted structure (Figure 4a).

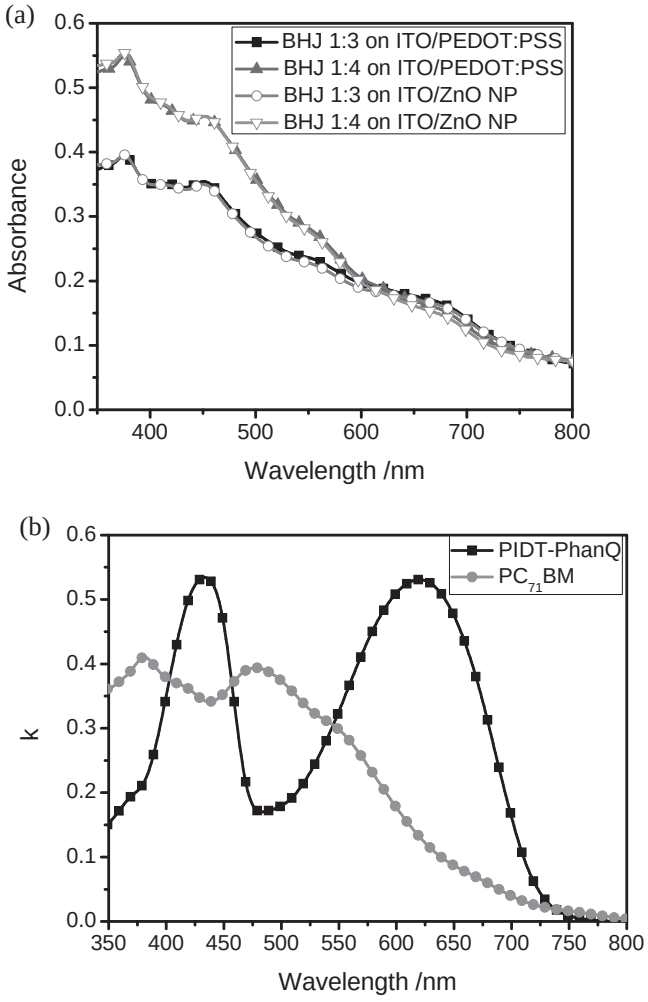

Figure 4. a) Direct absorption spectra of PIDT-PhanQ:$PC_{71}BM$ BHJ films with different content and substrates (reference on PEDOT/ITO and ZnO/ITO, respectively. b) Complex index of refraction imaginary part *k* for PIDT-PhanQ and $PC_{71}BM$.

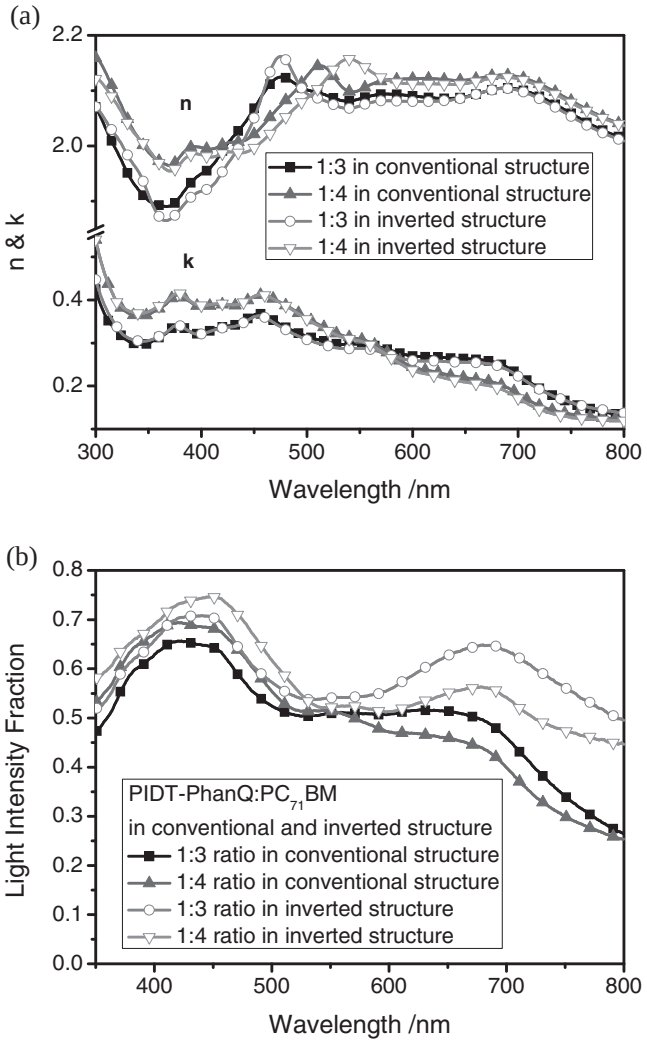

Figure 5. a) Optical constants and b) fraction of absorbed light intensity calculated by the transfer matrix optical model of PIDT-PhanQ:$PC_{71}BM$ films with 1:3 and 1:4 blending ratio in conventional and inverted structure devices.

However, the fraction of incident light intensity absorbed by the films is influenced by all layers in the device due to the interference effect, therefore, the independently measured absorption of BHJ films can not be counted on to represent the absorption of films in devices. To determine the individual contribution of the active layer on optical absorption, proper optical modeling is needed.[39] In this work, a transfer matrix formalism is used to calculate the interference of reflected and transmitted light waves at each interface in the stack based on the wavelength-dependent complex index of refraction ($n + ik$) of each material.[37,40,41] The imaginary part of the complex index of refraction (k) could be measured directly by UV-vis spectrometry and the real part (n) could be measured by variable angle spectroscopic ellipsometry for each layer (**Figure 5**a).

Based on the n and k values for each layer, the fraction of light absorbed by the BHJ films in both conventional and inverted device structures are calculated and summarized in Figure 5b. Due to the difference of layer sequence and the optical properties of ZnO NP, PEDOT:PSS, and metals, the BHJ films showed dramatically different intensities of absorption fraction within the conventional and inverted device structures despite having the same content and similar extinction coefficients. In general, the fractions of absorbed light in BHJ films of the inverted devices are greater when the active layer was kept with the same thickness. Although the optical constant is spatially dependent, the BHJ layer is treated as a homogenous film and its diffuse scattering is ignored in this optical modeling.

To facilitate the calculation of the maximum attainable photocurrents (J_{max}), 100% internal quantum efficiency (IQE) was assumed for all wavelengths. However, due to potential loss in charge recombination, transport, and collection, it is almost impossible to achieve 100% IQE, therefore, the experimental value of J_{sc} is always lower than that of the J_{max}. The calculated J_{max} values and ratio between J_{sc} and J_{max} are summarized in Table 1. For the conventional structure device with the 1:3 blending ratio, the calculated J_{max} value is 13.0 mA cm^{-2},

while the experimental J_{sc} value is 11.0 mA cm^{-2}, which indicates that ≈86% of the generated excitons have been converted into charges and harvested by the electrodes.

However, in the same BHJ film of the inverted devices, only 63% of the generated excitons contributed to the photocurrents. By increasing the fullerene content to 80% in the conventional structure, the J_{sc}/J_{max} ratio decreased slightly from 86% to 83%, while it increased from 63% to 71% in the inverted structure. Generally, the same thickness films with a 1:4 ratio generated fewer excitons than the 1:3 ratio films. The increased J_{sc}/J_{max} ratio in the inverted structure demonstrates that higher fullerene content is favored for better charge separation, transport, and collection.

To understand the necessity for higher fullerene content in the inverted structure devices, the spatial distribution of exciton generation in BHJ films was also calculated. As it shown in **Figure 6**, the generated excitons is broadly distributed within the BHJ film of the conventional device with its peak approximately in the center, while the excitons is concentrated mainly in the region, which is 40–80 nm away from the electron-transporting layer in the inverted device with its peak located near the top of the BHJ film.

In the latter case, most of the generated excitons are closer to the anode. Therefore, most of the generated electrons need to travel longer distance in order to be collected by the cathode. This increases the probability of charge recombination during their transport. The result of this modeling is consistent with the lower FF observed for inverted devices with 1:3 blending ratio. It also provides the explanation for higher fullerene ratio required in the inverted devices because it may provide a better-connected electron-transporting path in the device to decrease possible bimolecular recombination.

To prove that higher fullerene ratio can aid in electron transport and collection, both hole-only devices with the configuration of ITO/PEDOT:PSS/BHJ/Pd and electron-only devices with the configuration of ITO/Al/BHJ/Ca/Al were fabricated. **Figure 7** shows the log scale *J–V* characteristics in the dark for devices with the blending ratios of 1:3 and 1:4. Higher electron mobility was observed for the devices with 1:4 blending ratio, while hole mobility for the devices with 1:3 blending ratio was higher. The *J–V* curves were fitted with the space-charge-limited-current (SCLC) model to calculate both mobilities. The electron and hole mobility in the 1:3 ratio BHJ film is 3.68×10^{-5} cm^2 V^{-1} s^{-1} and 2.17×10^{-3} cm^2 V^{-1} s^{-1}, respectively. The electron mobility in the 1:4 ratio BHJ films was 1.06×10^{-4} cm^2 V^{-1} s^{-1}, which is about 3 times that of the 1:3 ratio BHJ film; while the hole mobility decreased to 1.00×10^{-3} cm^2 V^{-1} s^{-1}. Increasing the fullerene ratio significantly improved the electron mobility. Although it also slightly decreased the hole mobility, it is still much higher than the electron mobility. Due to the exciton generation peak shifting to anode in inverted structure, the electron mobility is more critical to prevent recombination loss. The mobility data shows that electron transportation is more

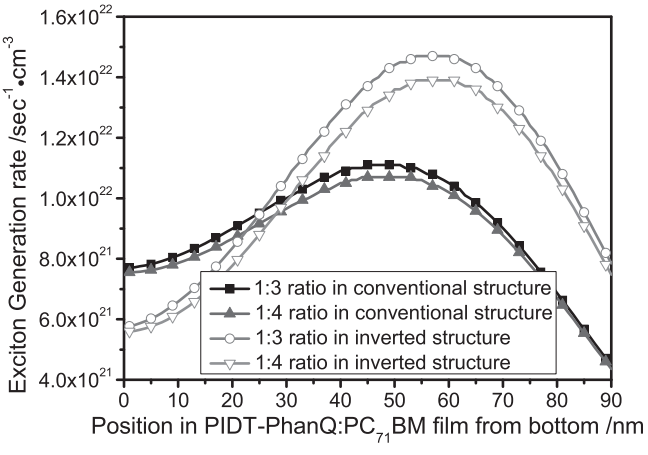

Figure 6. Calculated distribution profile of exciton generation rate in PIDT-PhanQ:PC$_{71}$BM film in PSCs with 1:3 and 1:4 blending ratio in conventional and inverted structure devices.

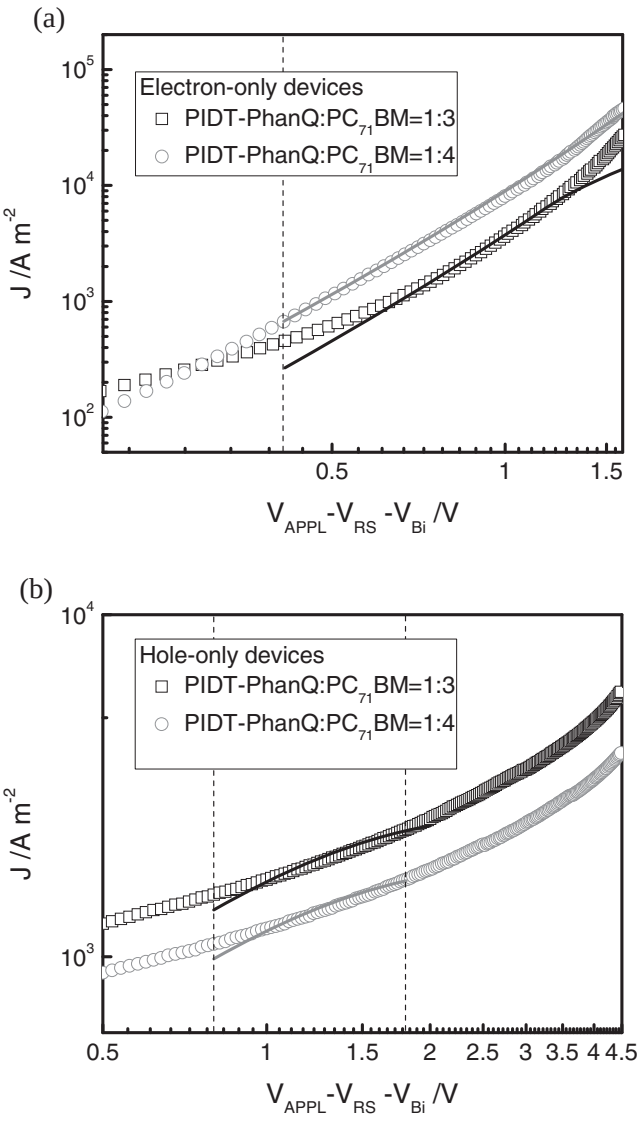

Figure 7. Measured *J–V* characteristics under dark for a) electron-only and b) hole-only devices consisting of PIDT-PhanQ/PC$_{71}$BM BHJ films. The bias (*V*) is corrected for built-in voltage, V_{Bi}, arising from difference in the work function of the contacts, and the voltage drop due to substrate's series resistance (V_{RS}), such that $V = V_{APPL} - V_{RS} - V_{Bi}$. ($V_{APPL}$ is the applied voltage).The solid lines represent the fitting curves.

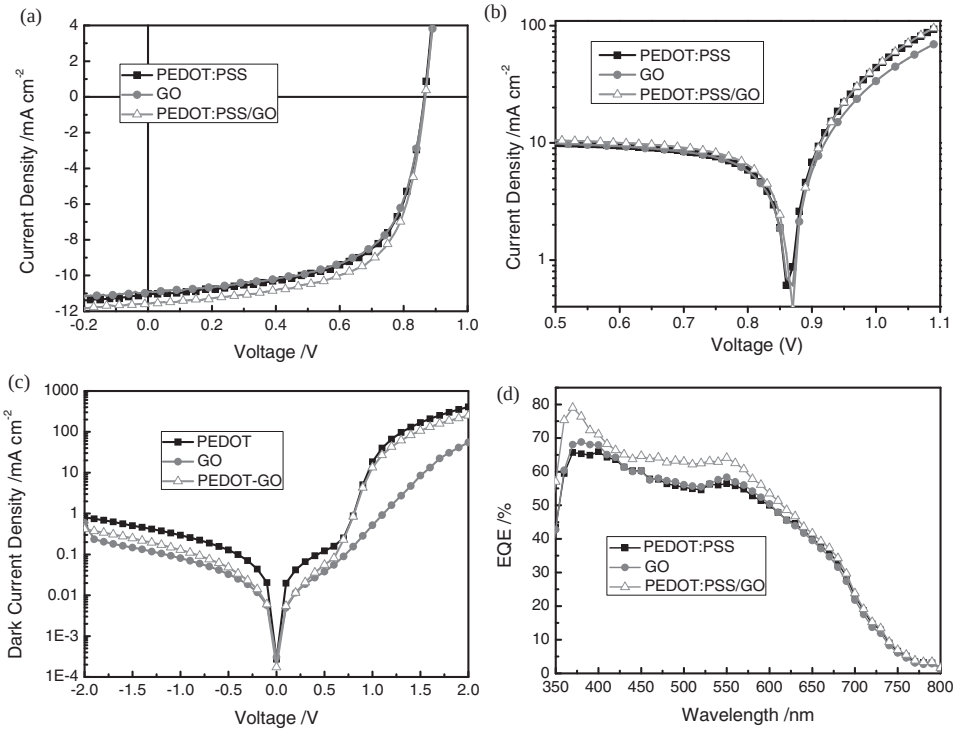

Figure 8. *J–V* characteristics of devices under illumination (a,b) and in the dark (c). d) EQE of devices with different hole-transporting top layers.

efficient in films with higher fullerene content. Mobility measurements based on the SCLC calculations are described in the Supporting Information. These data support the hypothesis that electrons are more efficiently transported in films with higher fullerene content.

2.3. Modification of the Hole-Transporting Layer

When PEDOT:PSS was used as hole-transporting layer in the 1:4 blending ratio inverted devices, PCE as high as 5.97% could be achieved. Recently, we have found that GO can function as a good anode interfacial layer to improve the performance of inverted cells.[20,42] To evaluate whether GO can be used to further improve the performance of inverted devices, hole-transporting layers based on individual PEDOT:PSS, GO, or their bilayer combination were investigated. The *J–V* characteristics of inverted cells are composed of different interfacial layers under illumination and in the dark, and their EQE data are shown in **Figure 8**. Their performance, with the series resistance (R_s) and the parallel resistance (R_p, or shunt resistance) are listed in **Table 2**. The devices utilizing a combined PEDOT:PSS (≈10 nm)/GO (≈2–3 nm) as hole-transporting layer show the best performance with J_{sc} of 11.6 mA cm^{-2} and PCE of up to 6.38%, which are comparable to those of the best conventional structure devices. The devices with GO as the interfacial layer show higher series resistance both under illumination and in the dark. However, they also give a lower leakage current in the dark under the reverse bias compared to PEDOT:PSS.

Table 2. Device performance of inverted structure PSCs with different hole-transporting layers.

Hole Transporting Layer	V_{oc} [V]	J_{sc} [mA cm^{-2}]	FF	R_s [Ω cm^2]	R_p [Ω cm^2]	PCE [%]
PEDOT:PSS	0.86	11.0	0.63	2.09	672	5.97
GO	0.86	10.9	0.62	2.87	672	5.88
PEDOT:PSS/GO	0.86	11.6	0.64	2.03	672	6.38

It is well known that PEDOT:PSS can not efficiently block electrons and it sometimes can even function as a cathode in PSCs to collect electrons.[43] By inserting a layer of GO, the electron-blocking properties of the anode buffer layer can be enhanced. After combining PEDOT:PSS and GO, a better electron-blocking effect was achieved for the device under reverse bias without sacrificing its low series resistance.

3. Conclusions

In summary, high-performance inverted devices based on PIDT-PhanQ/$PC_{71}BM$ have been demonstrated. The effects of device geometry on exciton harvesting and overall performance were investigated by using BHJ films processed under the same conditions. Higher fullerene blending ratios are needed in the inverted devices to achieve optimal PCEs. Optical modeling using a transfer matrix formalism has been utilized to explain the variations of performance in different device architectures. Different processing sequences and optical properties of buffer layers are shown to be responsible for the significant difference observed in optical field distribution and exciton generation profile throughout the devices. The shifted exciton generation peak position in inverted devices necessitates the higher ratio

of fullerene in the BHJ film to maintain adequate electron mobility. By utilizing a hole-transporting layer composed of PEDOT:PSS and GO, inverted structure PSCs with very high PCE of 6.38% has been demonstrated.

4. Experimental Section

Device Fabrication: PSCs were fabricated using ITO-coated glass substrates (15 Ω sq^{-1}), which were cleaned with detergent, deionized water, acetone, and isopropyl alcohol. In the conventional structure devices, a thin layer (≈35 nm) of PEDOT:PSS (Baytron P VP AI 4083, filtered at 0.45 μm) was first spin-coated on the pre-cleaned ITO-coated glass substrates at 5000 rpm and baked at 140 °C for 10 min under ambient conditions. The substrates were then transferred into a nitrogen-filled glovebox. Subsequently, the polymer:$PC_{71}BM$ active layer (≈90 nm) was spin-coated on the PEDOT:PSS layer from a homogeneous solution. The solution was prepared by dissolving the polymer and fullerene at different weight ratios in *o*-dichlorobenzene overnight and filtered through a PTFE (polytetrafluoroethylene) filter (0.2 μm). The substrates were annealed at 110 °C for 10 min prior to electrode deposition. At the final stage, the substrates were pumped down to high vacuum (<2 × 10^{-6} Torr), and calcium (30 nm) topped with aluminum (100 nm) was thermally evaporated onto the active layer. For inverted device fabrication, a thin layer of ZnO nanoparticles (≈30 nm) synthesized using the method described by Beek et al.[44] was spin-coated onto the pre-cleaned ITO-coated glass substrates. The same process used for active layer in the conventional structure devices was also used for the inverted devices. After annealing, PEDOT:PSS (10 nm) was spin-coated on top of BHJ film and annealed at 100 °C for 10 min. An Ag electrode (100nm) was then deposited to complete the inverted devices structure. Shadow masks were used to define the active area (10.08×10^{-2} cm^2) of the devices.

Device Characterization: The current–voltage (*J–V*) characteristics of unencapsulated photovoltaic devices were measured under ambient conditions using a Keithley 2400 source-measurement unit. An Oriel xenon lamp (450 W) with an AM1.5 G filter was used as the solar simulator. The light intensity was set to 1 sun (100 mW cm^{-2}) using a calibrated Hamamatsu silicon diode with a KG5 color filter, which can be traced to the National Renewable Energy Laboratory (NREL). The EQE system uses a lock-in amplifier (Stanford Research Systems SR830) to record the short-circuit current under chopped monochromatic light.

Supporting Information

Supporting Information is available from the Wiley Online Library or from the author.

Acknowledgements

The authors are thankful for support from the National Science Foundation (DMR-0120967), the Department of Energy (DE-FC3608GO18024/A000), the Air Force Office of Scientific Research (FA9550-09-1-0426), the Office of Naval Research (N00014-08-1-1129), and the World Class University (WCU) program at the Photovoltaic Materials, Department of Material Chemistry, Korea University through the National Research Foundation of Korea under the Ministry of Education, Science and Technology (R31-2011-000-10035-0). The variable angle spectroscopic ellipsometry instrumentation was provided by the Nanotechnology User Facility (NTUF), a member of the National Nanotechnology Infrastructure (NNIN) supported by NSF. Matlab code for transfer matrix optical model calculation was downloaded from Prof. Michael D. McGehee's group website. The authors also thank Dr. Ling Luo's help for the MATLAB code modification.

Received: December 5, 2011
Published online: March 29, 2012

[1] G. Yu, J. Gao, J. C. Hummelen, F. Wudl, A. J. Heeger, *Science* **1995**, *270*, 1789.
[2] S. Günes, H. Neugebauer, N. S. Sariciftci, *Chem. Rev.* **2007**, *107*, 1324.
[3] C. J. Brabec, J. R. Durrant, *MRS Bull.* **2008**, *33*, 670.
[4] B. C. Thompson, J. M. J. Frechet, *Angew. Chem. Int. Ed.* **2008**, *47*, 58.
[5] Y.-J. Cheng, S.-H. Yang, C.-S. Hsu, *Chem. Rev.* **2009**, *109*, 5868.
[6] J. Hou, H.-Y. Chen, S. Zhang, G. Li, Y. Yang, *J. Am. Chem. Soc.* **2008**, *130*, 16144.
[7] F. Huang, K.-S. Chen, H.-L. Yip, S. K. Hau, O. Acton, Y. Zhang, J. Luo, A. K.-Y. Jen, *J. Am. Chem. Soc.* **2009**, *131*, 13886.
[8] Y. Liang, Y. Wu, D. Feng, S.-T. Tsai, H.-J. Son, G. Li, L. Yu, *J. Am. Chem. Soc.* **2009**, *131*, 56.
[9] S. H. Park, A. Roy, S. Beaupré, S. Cho, N. Coates, J. S. Moon, D. Moses, M. Leclerc, K. Lee, A. J. Heeger, *Nat. Photonics* **2009**, *3*, 297.
[10] R. Qin, W. Li, C. Li, C. Du, C. Veit, H.-F. Schleiermacher, M. Andersson, Z. Bo, Z. Liu, O. Inganas, U. Wuerfel, F. Zhang, *J. Am. Chem. Soc.* **2009**, *131*, 14612.
[11] Y. Liang, Z. Xu,, J. Xia, S.-T. Tsai, Y. Wu, G. Li, C. Ray, L. Yu, *Adv. Mater.* **2010**, *22*, E135.
[12] Y. Zhang, S. K. Hau, H.-L. Yip, Y. Sun, O. Acton, A. K.-Y. Jen, *Chem. Mater.* **2010**, *22*, 2696.
[13] Y. He, H.-Y. Chen, J. Hou, Y. Li, *J. Am. Chem. Soc.* **2010**, *132*, 1377.
[14] M. Jorgensen, K. Norrman, F. C. Krebs, *Sol. Energy Mater. Sol. Cells* **2008**, *92*, 686.
[15] S. K. Hau, K. M. O'Malley, Y.-J. Cheng, H.-L. Yip, H. Ma, A. K.-Y. Jen, *IEEE J. Select. Topics Quantum Electron.* **2010**, *16*, 1665.
[16] S. K. Hau, H.-L. Yip, N. S. Baek, J. Zou, K. O'Malley, A. K.-Y. Jen, *Appl. Phys. Lett.* **2008**, *92*, 253301.
[17] A. K. K. Kyaw, X. W. Sun, C. Y. Jiang, G. Q. Lo, D. W. Zhao, D. L. Kwong, *Appl. Phys. Lett.* **2008**, *93*, 221107.
[18] C. Tao, S. Ruan, X. Zhang, G. Xie, L. Shen, X. Kong, W. Dong, C. Liu, W. Chen, *Appl. Phys. Lett.* **2008**, *93*, 193307.
[19] G. Li, C.-W. Chu, V. Shrotriya, J. Huang, Y. Yang, *Appl. Phys. Lett.* **2006**, *88*, 253503.
[20] Y. Gao, H.-L. Yip, S. K. Hau, K. M. O'Malley, N. C. Cho, H. Chen, A. K.-Y. Jen, *Appl. Phys. Lett.* **2010**, *97*, 203306.
[21] C. Waldauf, M. Morana, P. Denk, P. Schilinsky, K. Coakley, S. A. Choulis, C. J. Brabec, *Appl. Phys. Lett.* **2006**, *89*, 233517.
[22] M. S. White, D. C. Olson, S. E. Shaheen, N. Kopidakis, D. S. Ginley, *Appl. Phys. Lett.* **2006**, *89*, 143517.
[23] S. K. Hau, H. L. Yip, J. Zou, A. K.-Y. Jen, *Org. Electron.* **2009**, 1401.
[24] J. Zou, H.-L. Yip, S. K. Hau, A. K.-Y. Jen, *Appl. Phys. Lett.* **2010**, *96*, 203301.
[25] S. K. Hau, H.-L. Yip, O. Acton, N. S. Baek, H. Ma, A. K.-Y. Jen, *J. Mater. Chem.* **2008**, *18*, 5113.
[26] S. K. Hau, H.-L. Yip, H. Ma, A. K.-Y. Jen, *Appl. Phys. Lett.* **2008**, *93*, 233304.
[27] C.-H. Hsieh, Y.-J. Cheng, P.-J. Li, C.-H. Chen, M. Dubosc, R.-M. Liang, C.-S. Hsu, *J. Am. Chem. Soc.* **2010**, *132*, 4887.
[28] T. Yang, W. Cai, D. Qin, E. Wang, L. Lan, X. Gong, J. Peng, Y. Cao, *J. Phys. Chem. C* **2010**, *114*, 6849.
[29] T. Ameri, G. Dennler, C. Waldauf, P. Denk, K. Forberich, M. C. Scharber, C. J. Brabec, K. Hingerl, *J. Appl. Phys.* **2008**, *103*, 084506.
[30] T. Ameri, G. Dennler, C. Waldauf, A. Hamed, A. Seemann, K. Forberich, J. Hauch, M. Scharber, K. Hingerl, C. J. Brabec, *Adv. Funct. Mater.* **2010**, *20*, 1592.
[31] F. C. Chen, J. L. Wu, Y. Hung, *Appl. Phys. Lett.* **2010**, *96*, 193304.
[32] Z. Xu, L.-M. Chen, G. Yang, C.-H. Huang, J. Hou, Y. Wu, G. Li, C.-S. Hsu, Y. Yang, *Adv. Funct. Mater.* **2009**, *19*, 1227.

[33] C.-H. Hsieh, Y.-J. Cheng, P.-J. Li, C.-H. Chen, M. Dubosc, R.-M. Liang, C.-S. Hsu, *J. Am. Chem. Soc.* **2010**, *132*, 4887.
[34] K.-S. Chen, Y. Zhang, H.-L. Yip, Y. Sun, J. A. Davies, C. Ting, C.-P. Chen, A. K.-Y. Jen, *Org. Electron.* **2011**, *12*, 794.
[35] Y.-J. Cheng, C.-H. Hsieh, Y. He, C.-S. Hsu, Y. Li, *J. Am. Chem. Soc.* **2010**, *132*, 17381.
[36] Y. Sun, J. Seo, Ch. J. Takacs, J. Seifter, A. J. Heeger, *Adv. Mater.* **2011**, *23*, 1679.
[37] C. M. Amb, S. Chen, K. R. Graham, J. Subbiah, C. E. Small, F. So, J. R. Reynolds, *J. Am. Chem. Soc.* **2011**, *133*, 10062.
[38] Y. Zhang, J. Zou, H. L. Yip, K.-S. Chen, D. F. Zeigler, Y. Sun, A. K.-Y. Jen, *J. Mater. Chem.* **2011**, *23*, 2289.
[39] G. F. Burkhard, E. T. Hoke, M. D. McGehee, *Adv. Mater.* **2010**, *22*, 3293.
[40] L. A. A. Pettersson, L. S. Roman, O. Inganas, *J. Appl. Phys.* **1999**, *86*, 487.
[41] P. Peumans, A. Yakimov, S. R. Forrest, *J. Appl. Phys.* **2003**, *93*, 3693.
[42] Y. Gao, H.-L. Yip, K.-S. Chen, K. M. O'Malley, O. Acton, Y. Sun, G. Ting, H. Chen, A. K.-Y. Jen, *Adv. Mater.* **2011**, *23*, 1903.
[43] S. K. Hau, H. L. Yip, J. Y. Zou, A. K.-Y. Jen, *Org. Electron.* **2009**, *10*, 1401.
[44] W. J. E. Beek, M. M. Wienk, M. Kemerink, X. Yang, R. A. J. Janssen, *J. Phys. Chem. B* **2005**, *109*, 9505.